

Towards ultra-stable and dendrite-suppressed Li-metal batteries: Ion-regulating graphene-modified separators

Wootaeck Choi^a, Minsu Park^a, Sujeong Woo^a, Hyunwoo Kim^b, Min Sung Kang^d, Junghyun Choi^{c, **}, Sung Beom Cho^{d, ***}, Taehoon Kim^{b, ****}, Patrick Joohyun Kim^{a,*}

^a Department of Applied Chemistry, Kyungpook National University, Daegu, 41566, Republic of Korea

^b Composites Research Division, Korea Institute of Materials Science (KIMS), Changwon, 51508, Republic of Korea

^c School of Chemical, Biological and Battery Engineering, Gachon University, Seongnam-si, Gyeonggi-do 13120, Republic of Korea

^d Department of Materials Science and Engineering and Department of Energy Systems Research, Ajou University, Suwon-si, 16499, Republic of Korea

ARTICLE INFO

Keywords:

Lithium metal anode
Wettability enhanced graphene
Hydrophilic separator
Homogeneous Li-ion flux

ABSTRACT

The practical application of metallic lithium (Li) anodes is hindered by nonuniform Li deposition/dissolution, as well as poor electrochemical reversibility during cycling. To address these challenges, surface modification of polymer separators with functional materials has been extensively explored. In this study, two distinct surface-modifying layers composed of MnO_x and polydopamine (PDA) are applied to modify the surface of graphene-coated polypropylene separators (G@PP). Both MnO_x and PDA, which are formed through the graphene layer, significantly enhance the intrinsic electrolyte wettability of G@PP, resulting in a homogeneous Li-ion flux. Furthermore, the lithiophilic properties revealed by DFT and COMSOL analyses synergize with the hydrophilic characteristics, resulting in a more stable electrochemical performance in Li-metal batteries (LMBs). The enhanced electrolyte permeability of the coating layer allows Li–Cu cells with MnO_x -modified graphene-coated PP (MG@PP) and PDA-modified graphene-coated PP (PG@PP) separators to exhibit significantly improved cycle stability compared with Li–Cu cells with G@PP separators. Interestingly, Li–S cells equipped with MG@PP and PG@PP separators exhibit also enhanced electrochemical performance compared with Li–S cells with G@PP separators. These results highlight that surface engineering of separator-coating materials along with hydrophilic and lithiophilic materials enhances both long-term cycle stability and electrochemical kinetics in LMBs.

1. Introduction

The electric vehicle (EV) market is rapidly growing as combustion engine vehicles are replaced by EVs in response to accelerating global warming and carbon-neutral policies [1–3]. Extensive research has focused on advanced energy storage systems, aiming to achieve high energy density, high power density, and stable cycling performance [4, 5]. Theoretical studies on Li-metal batteries (LMBs) have been intensely promoted because of the low energy density of widely commercialized Li-ion batteries. Li-metal anodes are considered the “holy grail anode” of next-generation energy storage systems because of their ultrahigh theoretical capacity (3860 mAh g^{-1}), low density (0.59 g cm^{-3}), and low electrochemical potential (-3.04 V versus SHE) [6–8]. However, the

practical use of LMBs faces intrinsic challenges, including poor Coulombic efficiency (CE) and poor cycle stability due to dead Li formation, uncontrolled Li dendrite growth, and Li volume expansion [9–11].

The separator is a crucial battery component that prevents physical contact between the cathode and anode while facilitating Li-ion migration [12]. Beyond these basic functions, various strategies have been proposed to enhance the functionality of the separator by modifying its surface with functional groups or polymers and applying boehmite coatings [13–15]. These enhancements have significantly improved the cycle stability and electrochemical kinetics of Li-ion batteries. However, despite these improvements, these advanced separators are not ideal for LMBs because they cannot mitigate issues such as Li dendrite formation and low Coulombic efficiency [9–11].

* Corresponding author.

** Corresponding author.

*** Corresponding author.

**** Corresponding author.

E-mail addresses: junghchoi@gachon.ac.kr (J. Choi), csb@ajou.ac.kr (S.B. Cho), tkim67@kims.re.kr (T. Kim), pjkim@knu.ac.kr (P.J. Kim).

Nomenclature

| | |
|---------|--|
| (LMBs) | Li-Metal Batteries |
| (G) | Graphene |
| (G@PP) | Graphene-coated polypropylene |
| (MG@PP) | MnO _x -modified graphene-coated polypropylene |
| (PG@PP) | polydopamine-modified graphene-coated polypropylene |

Among the many options, graphene stands out for separator modification because of its high surface area, high electrical conductivity, low weight, and cost-effectiveness [16–19]. When a graphene-coated separator is used in Li-metal-based cells, it effectively reduces the local current density on counter electrodes and accommodates the volume change of Li during cycling [19–21]. Moreover, when graphene is coated on a separator facing the current collector, Li dendrites grow on the graphene layer, directing their growth toward the current collector. This directional growth prevents the Li dendrite from penetrating the separator, significantly enhancing the cycle performance of LMBs [22]. However, graphene has critical drawbacks due to its relatively limited electrolyte wettability and lithiophobic nature [23–25]. These features result in a relatively nonuniform Li-ion flux and Li deposition, which accelerate dendritic Li growth and electrolyte consumption in LMBs [23, 26].

Electrolyte wettability plays a critical role in LMBs by ensuring uniform infiltration and optimal contact with active materials, thereby enhancing ionic conductivity and reducing internal resistance [18, 27, 28]. Improved wettability facilitates uniform Li plating, which is crucial for minimizing Li dendritic formation and improving the electrochemical reversibility [26]. These features contribute to extended cycle life and high-rate performance in LMBs.

To address these inherent weaknesses of the graphene layer on the PP separator, this study demonstrates the surface decoration of G@PP separators with functional organic and inorganic layers via solution coating. MnO_x, a metal oxide, and PDA, an organic material, have been adopted as lithiophilic and hydrophilic agents [29, 30]. The improved electrolyte wettability of G@PP achieved through MnO_x and PDA coatings significantly enhances ionic conductivity and the homogeneity of Li-ion flux [28, 31–34]. Additionally, previous studies have shown that MnO_x enhances its lithiophilic characteristics by converting into an Mn/LiO₂ nanocomposite after initial lithiation [35, 36]. This conversion facilitates a uniform distribution of Li-ion flux during the Li deposition process. PDA is recognized as a lithiophilic material because of its strong adsorption energy for Li-ions, resulting from Lewis acid-base interactions [37]. These material features contribute to the improved electrochemical performance of LMBs by enabling uniform Li deposition and dissolution across both electrodes. Due to the synergistic contributions of each surface-modifying material, excellent cycle stability of both LMBs and Li-S batteries has been successfully demonstrated. These results were thoroughly examined through experimental analyses and COMSOL multi-physics simulations.

2. Materials and methods

2.1. Preparation of the G@PP, MG@PP, and PG@PP

A slurry for G@PP was prepared by mixing 0.45 g of graphene nanosheet powder, with particle sizes ranging from 5 to 25 µm (Graphene Supermarket), and 10 wt% binder (polyvinylidene fluoride (PVDF)) in 1-methyl-2-pyrrolidone (NMP, 99.5 %, SAMCHUN) using a planetary mixer (AR-100, THINKY) at 2000 rpm for 10 min. The resulting slurry was then cast onto a PP separator and dried in an oven at 50°C for 12 h.

The MG@PP separator was produced using the solution floating method. A solution of 0.0005 M KMnO₄ (Sigma-Aldrich) in DI water was introduced into a glass vial. Subsequently, G@PP was floated on the solution, and the vial was then placed in an oven at 50°C for 48 h. The resulting MG@PP was washed with DI water at least three times and then dried in an oven for 6 h. Finally, the separator was punched into circular discs with an 18 mm diameter.

The PG@PP separator was also fabricated using the solution floating method. Initially, the pH of a 0.1 M trizma® hydrochloride (Sigma-Aldrich) solution in DI water was adjusted to 8.5 by adding a 0.6 M sodium hydroxide bead (NaOH, >98.0 %, SAMCHUN) solution. A dopamine solution was then prepared by dissolving 0.02 mol of dopamine hydrochloride (Sigma-Aldrich) in a mixture of tris buffer solution and methanol (SAMCHUN) in a 1:1 vol ratio. G@PP was subsequently floated on this dopamine solution at 25°C for 48 h. The resulting PG@PP was washed with DI water at least three times and then dried in an oven for 6 h. Finally, the separator was punched into circular discs with an 18 mm diameter.

2.2. Fabrication of Li-Cu cells and Li-S full cells

Electrochemical tests for PP, G@PP, MG@PP, and PG@PP within Li-Cu cell systems were conducted using CR2032-type coin cells, which possess a diameter of 16 mm and use 1.0 T Li metal foil. The Cu foil utilized had a diameter of 12 mm and a thickness of 20 µm. These cells employed a PP separator (Celgard 2400) and an electrolyte consisting of 1.0 M LiPF₆ in EC:DEC at a 1:1 vol ratio. Sulfur electrodes were prepared by mixing 60 wt% sulfur powder (Sigma-Aldrich), 30 wt% Super P, and 10 wt% polyvinylidene fluoride (PVDF) binder in NMP solvent using a mixer. The resulting slurry was then cast onto an Al foil and dried at 50°C for 24 h. Subsequently, the foil was punched into circular electrodes with a diameter of 12 mm and an areal mass loading of approximately 1.5 mg cm⁻². The Li-S full cell tests were conducted across a voltage range of 1.7–2.8 V, employing an electrolyte composed of 1.0 M LiTFSI in (DOL:DME) (1:1 by volume) with LiNO₃ additive. All cells were assembled in an argon-filled glovebox, maintaining O₂ and H₂O levels below 0.1 ppm.

2.3. Characterizations

Surface morphology analysis of PP, G@PP, MG@PP, and PG@PP was performed using field emission scanning electron microscopy (FE-SEM; Hitachi SU8230) coupled with corresponding energy-dispersive X-ray spectroscopy (EDS, Ultim Max100, OXFORD). Before examining the morphology of Li nucleation and dendrite growth, the cells were disassembled in the glovebox and then rinsed in DEC to remove residual Li salts. X-ray photoelectron spectroscopy (XPS) profiles were obtained using an X-ray photoelectron spectrometer (Thermo Fisher NEXSA). Thermogravimetric analysis (TGA) was performed using an auto-thermogravimetric analyzer (TA Instruments, Discovery SDT 650). Fourier transform infrared spectroscopy (FT-IR, IR Prestige-21, Shimadzu) was utilized in the wavelength range of 600–4000 cm⁻¹. To analyze the crystallographic structures of the samples, X-ray diffraction (XRD, Panalytical, EMPYREAN) measurement was conducted. Electrochemical performance assessments were conducted using a battery tester (CT-4008Q-5 V100 mA-124, Neware). Electrochemical impedance spectroscopy (EIS) was performed across a frequency range of 10 mHz–200 kHz at an amplitude of 10 mV using a VSP system from Biologic, Seyssinet-Pariset. The Li-ion diffusion coefficient was determined using a galvanostatic intermittent titration technique (GITT, WBCS3000L32, WonATech), applying a pulse current of 0.2 mA cm⁻² for 10 min followed by a relaxation time of 10 min in a voltage window of 0.001–1.0 V (vs Li/Li⁺). The contact angle was measured to assess the wettability of each coating layer using a contact angle measuring instrument (Phoenix300 Touch, SEO).

2.4. DFT calculations

Density functional theory (DFT) calculations using the Vienna ab-initio simulation package (VASP) were conducted to understand the adsorption characteristics of graphene, MnO_2 , and PDA on Li [38]. These analyses employed the projector-augmented wave method and the exchange-correlation potential described by the generalized gradient approximation (GGA) within the Perdew-Burke-Ernzerhof (PBE) parametrization [39,40]. The plane-wave basis set was expanded to a cutoff energy of 520 eV to reduce the Pulay stress during structural optimization. The Brillouin zone was sampled using a density of 100 k-points per \AA^3 of reciprocal cell. The adsorption energy (E_{ads}) of Li on the surfaces was determined as follows:

$$E_{\text{ads}} = E_{\text{System}} - E_{\text{Surface}} - E_{\text{Li}} \quad (1a)$$

Where E_{Surface} and E_{Li} represent the energy of the substrate surface and the isolated Li atom, respectively, and E_{System} denotes the total energy of the Li-substrate surface.

2.5. FEM simulation

The modeling of Li dendrite growth on the separator and the distribution of current density in the cells was conducted using the COMSOL Multiphysics 6.2 software based on Finite Element Methods (FEMs). In this modeling approach, the current distribution, mass transport, and electrochemical reactions were coupled together. Three modules (transport of diluted species, secondary current distribution, level set) in COMSOL were used to solve the electrochemical deposition modeling. For Li dendrite growth, the cathode and anode potentials were set to -0.1 and 0.1 V, respectively, and the exchange current density was fixed at 100 A m^{-2} . The detailed parameters used in the simulation and their values are described in Table S1.

3. Results and discussion

Fig. 1 illustrates a comparison of the mechanisms by which a G@PP and a wettability-enhanced graphene-coated separator affect the behavior of the Li deposition process. The graphene coating on the separator reduces the overall current density applied to the counter electrode and disperses the localized heat generated at the interface between the counter electrode and the separator. However, the inefficient electrolyte permeability of G@PP results in an inhomogeneous Li-ion distribution across the coating layer (**Fig. 1a**). As Li ions repeatedly migrate across the graphene layer, Li dendrites eventually grow over the

electrode, leading to safety issues such as battery short circuits. The enhanced electrolyte wettability of the graphene layer achieved through surface modification with hydrophilic materials provides more pathways for Li-ion diffusion, promoting a homogeneous Li-ion flux (**Fig. 1b**). Consequently, less sharp dendritic Li forms over the electrode due to uniform Li deposition. Uniform Li deposition significantly reduces the risk of battery short circuits and improves the electrochemical reversibility of the Li deposition/dissolution process.

Fig. 2a shows a schematic illustration of the fabrication of the MG@PP and PG@PP separators. Initially, G@PP was created by tape-casting a graphene slurry onto a conventional PP separator. Surface modification of G@PP was then performed by suspending it in KMnO_4 and PDA solutions, resulting in the coating of MnO_x and PDA on the graphene surface, respectively. Finally, the obtained MG@PP and PG@PP separators were washed multiple times with DI water. Surface characterization of the PP, G@PP, MG@PP, and PG@PP separators was performed using SEM and EDS analyses. As shown in **Fig. 2b**, the PP separator has many pores across its surface. **Fig. 2c–e** illustrate the morphology of graphene on G@PP. The graphene laminated on the PP separator exhibits a plate-like 2D structure, which helps reduce the local current density and is coated with a thickness of $20 \mu\text{m}$. **Fig. 2f and g** demonstrate that MG@PP has a uniform coating of MnO_x on G@PP. MnO_x displays a flake-like morphology on graphene, similar to the forms observed in other studies [41]. Furthermore, the EDS mapping images in **Fig. 2h and i** illustrate the successful and uniform distribution of MnO_x on graphene, as indicated by the respective distributions of Mn and O. Meanwhile, PDA remains invisible in the SEM images, as it disperses into a thin layer without forming aggregates when lightly coated (**Fig. 2j and k**) [42]. The successful fabrication of PG@PP was confirmed by the presence of nitrogen in the EDS mapping images, indicating the formation of a uniform PDA polymer layer on graphene (**Fig. 2l and m**). **Figs. S1 and S2** demonstrate that the additional coating on the graphene does not increase its thickness.

To determine the content of the coated layer on each separator, thermogravimetric analysis (TGA) was performed under air flow using the powder obtained by scraping the separators (**Fig. 2n**). Initially, G powder from the G@PP separator shows a slight mass loss of around 200°C , which is associated with the vaporization of the NMP solvent. Subsequently, a slight mass reduction is observed between 200°C and 300°C , which is attributed to the decomposition of some labile oxygen-containing groups in the powder. A decrease in the TGA curve is noted around 360 – 600°C , which is attributed to the decomposition of PVDF. The curvature of the TGA graph shifts around 410°C , revealing the two-step decomposition pattern of PVDF. The mass percentage of the G

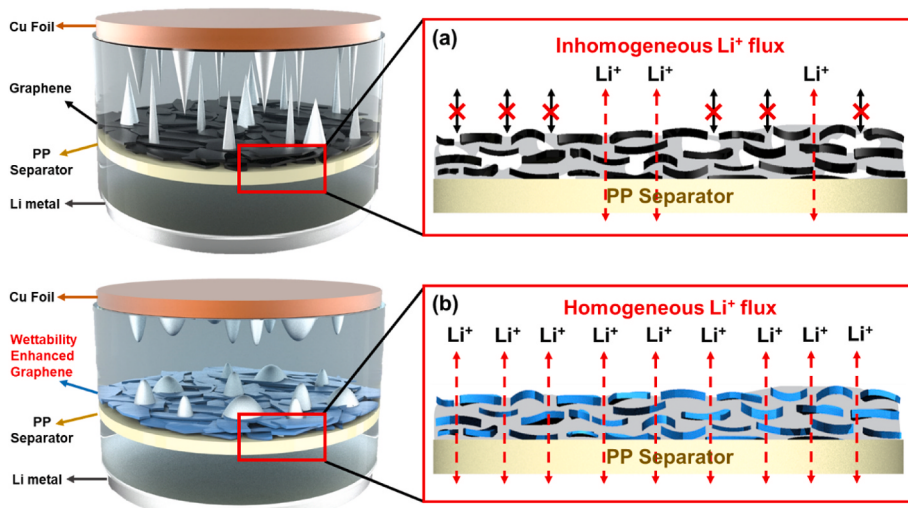


Fig. 1. Schematic illustration of (a) a graphene-coated separator and (b) a wettability-enhanced graphene-coated separator and their Li-ion flux mechanisms.

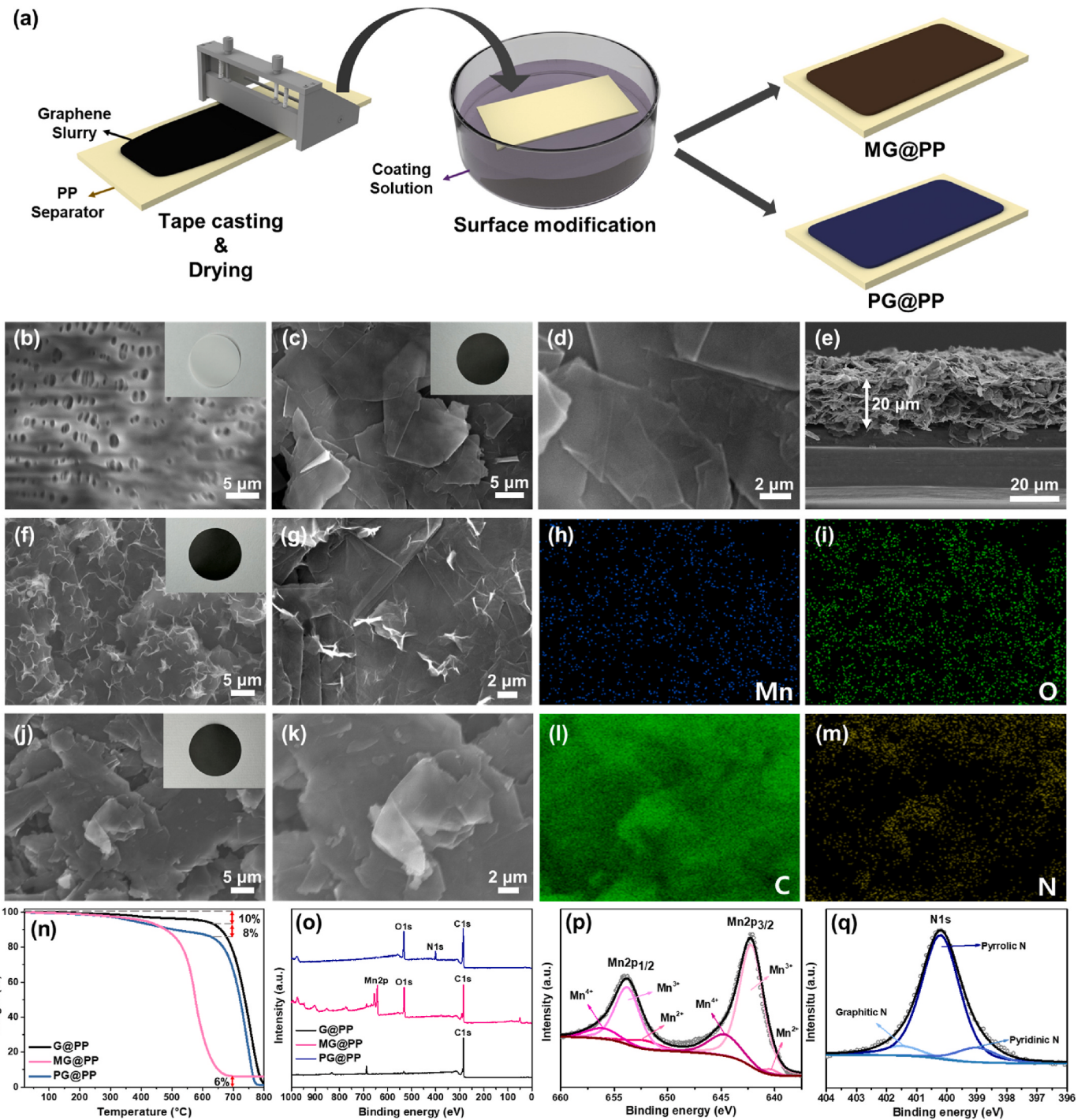


Fig. 2. (a) Process of surface modification with MG/PG on the polymer separator. Top-view SEM images of (b) the PP separator, (c and d) G@PP, (f and g) MG@PP, and (j and k) PG@PP. (e) Cross-sectional SEM image of G@PP. EDS mapping of (h and i) MG@PP and (l and m) PG@PP. (n) TGA curves and (o) XPS survey scan of each separator. XPS spectra of (p) Mn2p from MG@PP and (q) N1s from PG@PP.

powder rapidly drops by approximately 90 % starting at 650°C, indicating decomposition solely attributable to graphene without residual. Second, the TGA curve of PG, which was stripped from the PG@PP separator, reveals the content of PDA. Because of the multistep degradation of PDA initiated at 280°C, PG exhibit a mass percentage approximately 8 % lower than that of G at 650°C. This finding suggests that PG@PP is coated with 8 % PDA. Above 650°C, a decline in the curve occurs, similar to the decomposition behavior of G without any residual. Third, the mass ratio of the MG powder obtained from the MG@PP separator decreases at lower temperatures compared with the two

previously analyzed samples. This occurrence arises from mass loss attributed to oxygen release correlated with the transition of MnO₂ into Mn₂O₃, resulting in a lower valence of Mn [43]. MG yields a surplus of 6 %, indicating noncombusted remnants of Mn₂O₃. Based on these findings regarding the mass of released oxygen, it can be inferred that approximately 8 % of the coating factor has been applied to the separators, with a similar mass distribution.

Substances on the graphene sheet were identified using XPS survey scans. The wide XPS spectra indicate the overall peaks for G@PP, MG@PP, and PG@PP (Fig. 2o). Specific peaks appear in both MG@PP

and PG@PP compared with G@PP, which can be attributed to the coated substances on their surfaces. In the MG@PP curve shown in Fig. 2p, the main peaks of Mn $2p_{1/2}$ and Mn $2p_{3/2}$ appear at 654.08 and 642.78 eV, respectively, with a separation value of 11.3 eV, consistent with previous reports. Additionally, the primary peaks can be divided into three subpeaks corresponding to Mn $^{2+}$, Mn $^{3+}$, and Mn $^{4+}$, indicating

the diverse oxidation states of the transition metal Mn and the formation of MnO $_x$ on graphene. Meanwhile, in the XPS spectrum of PG@PP (Fig. 2q), the main peak of N1s is observed at 400.2 eV, which can be decomposed into three peaks corresponding to pyridinic N, graphitic N, and pyrrolic N. This demonstrates that nitrogen is well modified on carbon, indicating the successful coating of PDA on G@PP.

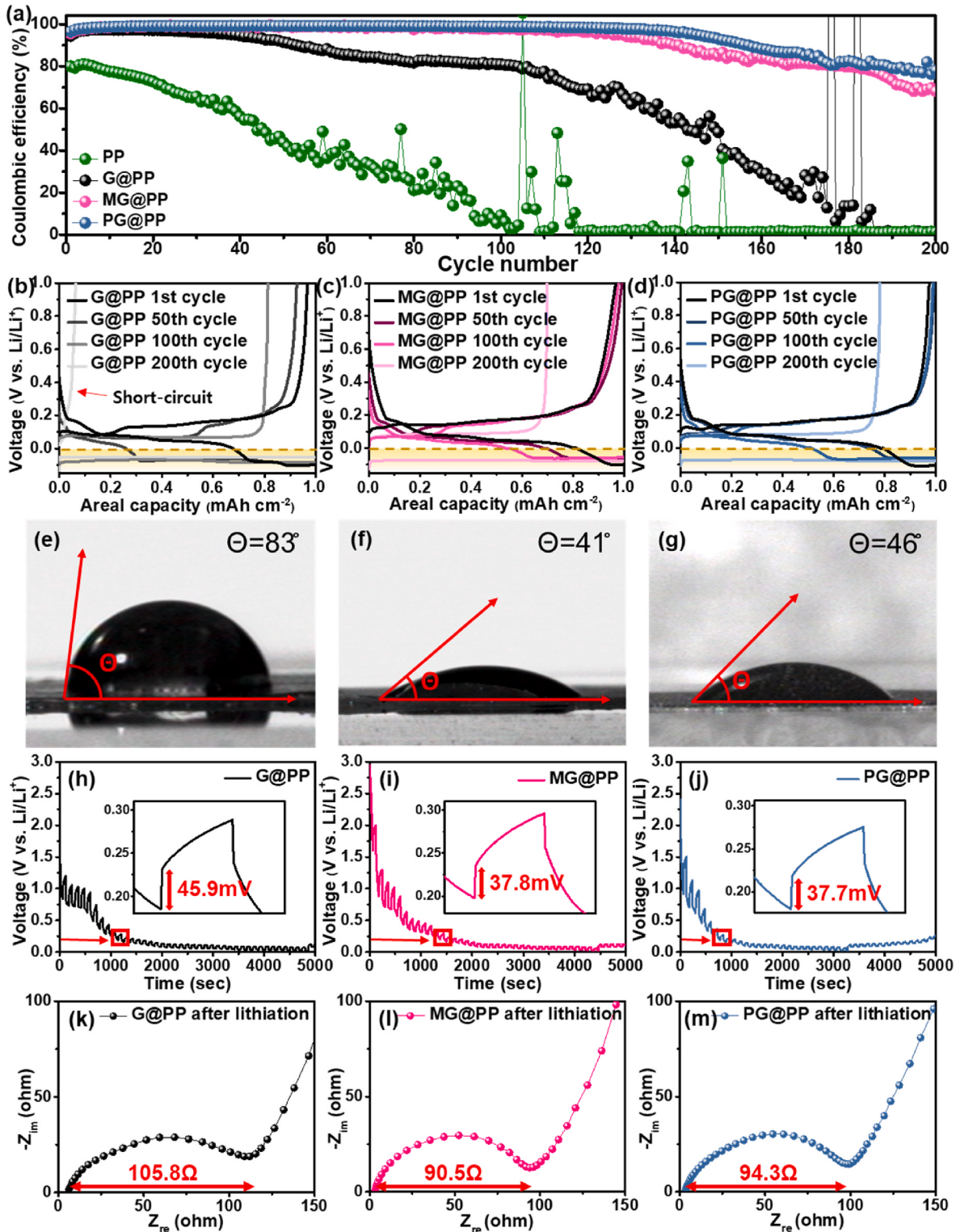


Fig. 3. Electrochemical performance of the Li-Cu cells. (a) Cycling performance of the cells with G@PP, MG@PP, and PG@PP at a current density of 2 mA cm $^{-2}$ and an areal capacity of 1 mAh cm $^{-2}$. (b–d) Voltage profiles of each cell at the 1st, 50th, 100th, and 200th cycles. Contact angle measurements of distilled water on (e) G@PP, (f) MG@PP, and (g) PG@PP. (h–j) GITT curves of each cell with different separators. (k–m) Nyquist plots after lithiation of each cell with different separators.

To further validate the coating of PDA and MnO_x on graphene, XRD and FT-IR analyses were conducted. In the XRD patterns shown in Fig. S3a, the graphs of G@PP and PG@PP exhibit no significant differences, with peaks related to PP being commonly observed. However, in the case of MG@PP, several distinct peaks are observed, which can be aligned with the tetragonal crystalline phase structure characteristic of $\alpha\text{-MnO}_2$, as referenced by JCPDS #44–141. In the FT-IR spectra shown in Fig. S3b, when compared to G@PP, PG@PP exhibits distinct peaks in the range of 1550 to 1450 cm^{-1} , which are associated with the C=C resonance vibration and N-H bending vibration observed in PDA. Additionally, MG@PP shows a peak at a wavenumber of 600 cm^{-1} , corresponding to the vibration of the Mn-O bond.

To investigate how the additional coating layer on G@PP affects the electrochemical stability and performance of LMBs, Li–Cu half cells were evaluated at a current density of 2 mA cm^{-2} and an areal capacity of 1 mAh cm^{-2} . To eliminate any synergistic effects from electrolyte additives, no additives were included in the tested electrolyte. Fig. 3a shows the cycling data of the Li–Cu half cells. The CE of the Li–Cu cell with the PP separator exhibits an initial Coulombic efficiency (ICE) of 80.1 %, which decreases to below 20 % after 86 cycles due to the growth of dendritic Li and the formation of dead Li. Owing to the reduced local current density from the graphene, the ICE of the cell with G@PP increases to 94.5 %. However, after the initial cycle, the CE gradually decays due to the uneven Li-ion flux. The CE significantly decreases after 100 cycles, reaching 18.9 % by the 167th cycle. In contrast, cells with MG@PP and PG@PP exhibit higher ICE of 95.7 % and 96.5 %, respectively, due to their assigned lithiophilic properties [44]. Furthermore, they maintain stable CE even after 100 cycles compared with cells with G@PP. They show CEs of 68.2 % and 78.1 %, respectively, after 200 cycles because both cells formed less dendritic Li and experienced a homogeneous Li-ion flux.

The 50th, 100th and 200th galvanostatic discharge/charge voltage profiles are compared to verify the electrochemical reversibility of each cell with different separators (Fig. 3b–d). In the cell with PP, the voltage drops below 0 V during the 1st discharge cycle, indicating the initiation of Li plating on copper as the discharge process starts (Fig. S4). Subsequently, at the 50th, 100th and 200th cycles, the discharge curve of the cell with PP exhibits a capacity value close to zero, declining almost vertically, indicating a short circuit. Meanwhile, plateaus near 0.17 V and 0.1 V appear during the 1st discharge in the cell with G@PP, as the voltage does not drop immediately below 0 V. These plateaus correlate with the lithiation reaction of the graphene nanosheet [18]. Subsequently, Li plating occurred on both copper and graphene below 0 V [22]. However, during the 100th and 200th cycles, no voltage profile related to the previously mentioned lithiation is observed. Instead, only Li plating occurred because of the irreversible deposition/dissolution of Li on the graphene. A significant decrease in capacity is observed compared to that at the 1st cycle, accompanied by amplified polarization, indicating a prominent decrease in reversibility. In the cells with MG@PP and PG@PP, plateaus corresponding to lithiation are also evident at 0.1 V and 0.17 V during the 1st cycle. Unlike in the cell with G@PP, the voltage profiles for MG@PP and PG@PP in their 1st, 50th, 100th and 200th cycles exhibit relatively similar shapes. Furthermore, because of the lithiophilic properties of the materials applied to the graphene, more uniform Li accommodation on the graphene was achieved. As a result, longer plateaus are observed in the lithiation regions. These findings stem from the increased reversibility, which is facilitated by the synergistic effect of hydrophilic and lithiophilic characteristics of the additional coating substances on the graphene layer.

To demonstrate the impact of MnO_x and PDA on electrolyte wettability, contact angle analysis was performed (Fig. 3e–g). Equal amounts of a polar solvent (e.g., DI water) were dropped onto each separator to measure the contact angle. The separators coated with MG and PG exhibit lower contact angles (41° and 46° , respectively) than the G@PP separator (83°). These results indicate higher polar solvent affinity and improved wettability due to the presence of hydrophilic MnO_x and PDA

coating layers. Higher affinity with the polar solvent primarily enhances wettability across the separator, leading to improved overall Li-ion diffusivity and additional Li-ion pathways [28].

To assess the Li-ion conductivity of the Li–Cu cells of each separator, GITT analysis was performed (Fig. 3h–j). At the same y-axis value, the IR drop for MG@PP and PG@PP (37.8 and 37.7 mV, respectively) is lower than that for G@PP (45.9 mV). This observation confirms that additional coating with hydrophilic materials improves the ionic conductivity of the graphene layer. The Li-ion diffusion coefficient of each cell was calculated using Fick's second law, which is expressed by the following equation:

$$D_{\text{Li}^+} = \frac{4}{\pi \tau} \left(\frac{m_b}{\rho S} \right)^2 \left(\frac{\Delta E_s}{\Delta E_t} \right)^2 \quad (1b)$$

where τ represents the duration time; S is the area of each separator; ρ is the density; m_b is the molar mass of the host material; ΔE_t and ΔE_s denote the steady-state and excess voltage variations, respectively, throughout each single galvanostatic titration step. The average Li-ion diffusion coefficients for the cells with G@PP, MG@PP, and PG@PP are 1.36×10^{-10} , 2.02×10^{-10} and $2.12 \times 10^{-10} \text{ cm}^2 \text{ s}^{-1}$, respectively. It is verified that the cells with MG@PP and PG@PP exhibit better Li-ion diffusivity than the cells with G@PP.

The EIS results for the separators are directly compared to highlight the difference in charge transfer resistance after the initial lithiation (Fig. 3k–m). Notably, the MG@PP and PG@PP separators exhibit smaller charge transfer resistances (90.5 and 94.3 Ω , respectively) than the G@PP separator (105.8 Ω). By extrapolating from the GITT and EIS measurements, the MG@PP and PG@PP separators exhibit enhanced Li-ion diffusivity compared with the G@PP separator. This improvement arises from the formation of efficient ion/electron transport pathways originating from the hydrophilic material coating on graphene. As the electrolyte wettability on graphene improves, the pathways for Li ions increase, resulting in more uniform Li deposition. Consequently, the dendritic growth of Li is inhibited because of consistent and homogeneous Li deposition and dissolution.

To investigate the effect of each separator on cycle stability under harsh conditions, each cell was tested under two sets of operating conditions: 8 mA cm^{-2} /1 mAh cm^{-2} and 2 mA cm^{-2} /3 mAh cm^{-2} . Initially, at 8 mA cm^{-2} /1 mAh cm^{-2} , the cell with PP (Fig. 4a) exhibits a gradual decrease in CE up to the 25th cycle, followed by a sharp decline. Subsequently, at the 58th cycle, the CE reaches a value of 14.3 %, resulting in a short circuit. The cell with G@PP exhibits better performance than that with PP because of the reduced local current density attributed to the presence of the graphene layer. It exhibits a steady decrease in CE up to the 41st cycle, reaching 72.4 %. However, beyond that point, the CE rapidly declines, reaching 16.9 % at the 64th cycle, resulting in a short

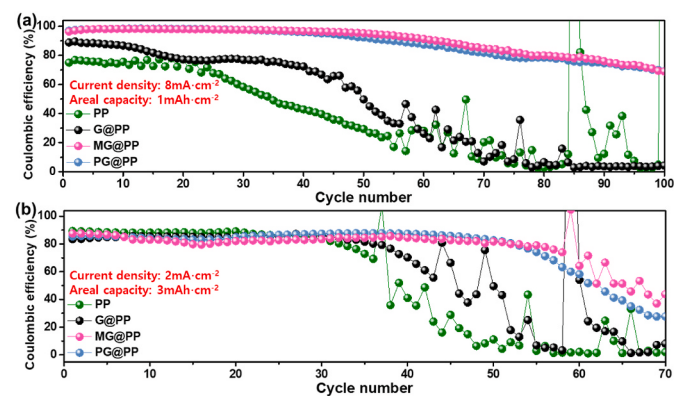


Fig. 4. Electrochemical stability tests at higher current densities and capacities. Cycling performance at (a) 8 mA cm^{-2} /1 mAh cm^{-2} and (b) 2 mA cm^{-2} /3 mAh cm^{-2} .

circuit. In contrast, cells with MG@PP and PG@PP initially achieve CEs exceeding 96 %. These cells demonstrate stable cycle retention for over 40 cycles, followed by a gradual overall decrease without short circuits. After 100 cycles, the MG@PP and PG@PP cells demonstrate excellent CEs of 69.0 % and 69.1 %, respectively. Fig. S5 illustrates that the cell with G@PP exhibits a more stable voltage profile compared to the one with PP. Furthermore, despite the rapid deposition/dissolution of Li, the cells with MG@PP and PG@PP exhibit even more stable voltage profiles. Hydrophilic modification of G@PP with MnO_x and PDA enhances efficient Li-ion migration, resulting in uniform Li-ion flux. Consequently, this modification leads to a high CE retention even at elevated current densities.

Similarly, under the conditions of $2 \text{ mA cm}^{-2}/3 \text{ mAh cm}^{-2}$ (Fig. 4b), the cell using a PP separator experienced a short circuit at the 37th cycle due to the penetration of Li dendrites through the separator. The CE of the cell with G@PP steadily decreases up to the 43rd cycle, resulting in the occurrence of a short circuit. In contrast, the cell with MG@PP remains stable until the 58th cycle before experiencing a short circuit. Simultaneously, cell with PG@PP shows consistent lifespan characteristics until the 54th cycle, after which a rapid decrease in CE led to cell decay. Fig. S6 further demonstrates that imparting hydrophilic properties to the separator results in a more stable performance even in high-capacity cells. The voltage profiles of the cells with PG@PP and MG@PP

exhibit more buffered and stable graph patterns than those with PP and G@PP. This observation indicates that even with increased Li loading, the enhanced wettability and lithiophilicity of G@PP suppress the growth of Li dendrites.

To investigate the effects of endowing the lithiophilic properties upon the graphene surface on the wettability, density functional theory (DFT) calculations were executed to study the adsorption energies between Li and functional groups. As shown in Fig. 5a–c, the binding energy of Li on the surface modified with MnO_2 and PDA is calculated to be -3.31 eV and -1.25 eV , respectively, while the pristine graphene surface has an adsorption energy of 0.74 eV . The calculated results validate a robust interaction between Li and lithiophilic materials, suggesting a high lithiophilicity of the surface modified with MnO_2 and PDA. Therefore, it demonstrates that the interaction with Li enhanced by the surface modification of the separator can improve the lithiophilicity and facilitate the uniform transportation of Li.

Additionally, to gain insights into the uniform Li-ion flux when the separator is modified to be hydrophilic, we used COMSOL Multiphysics to simulate the current density distribution, which reflects the distribution of Li ions. In the simulations, enhanced wettability is represented as an increase in the number of sites on the separator surface that interact with Li, considering the quantitative nature of wettability. For example, a low wettability separator was configured to have more

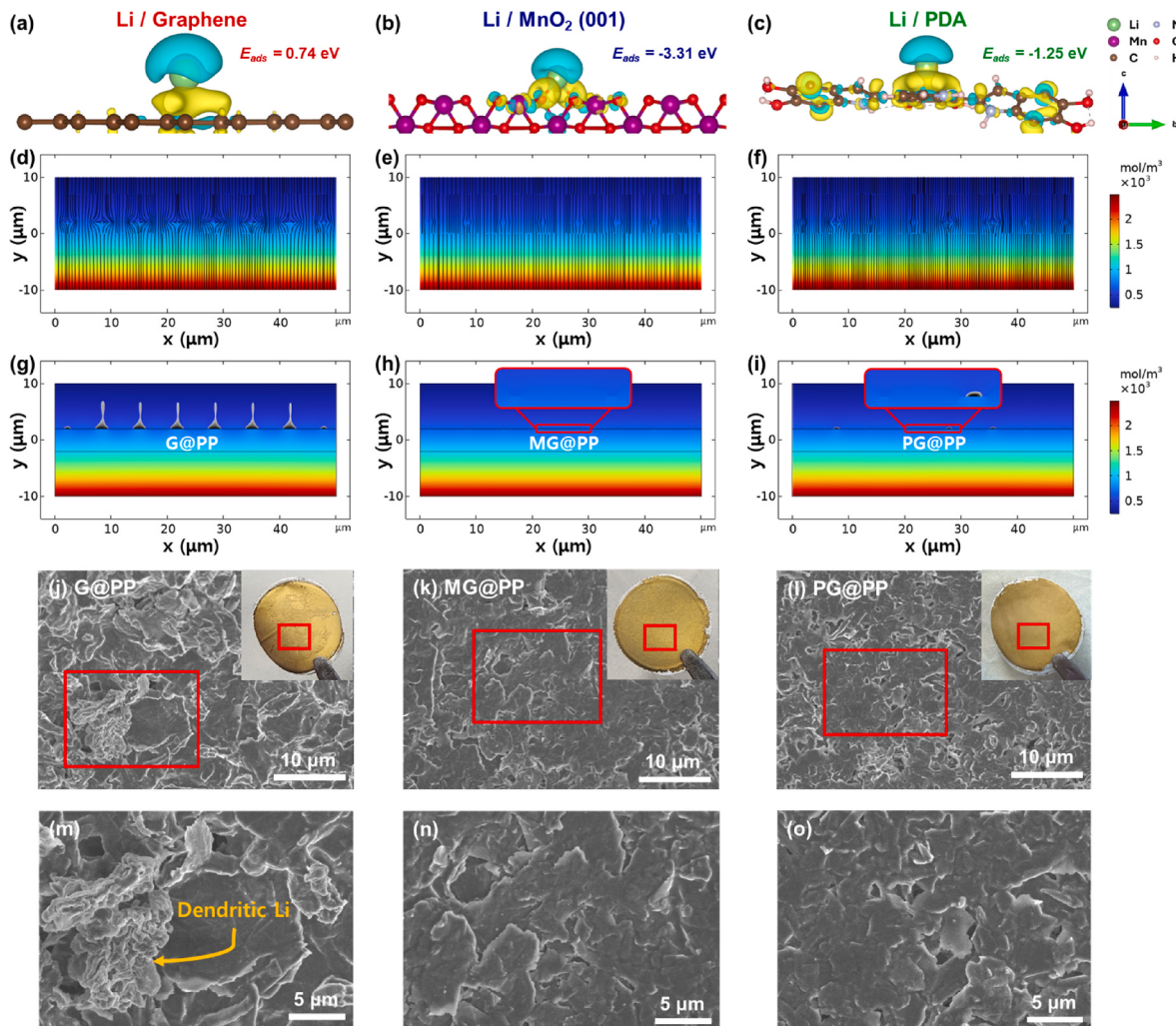


Fig. 5. The Li adsorption energy on (a) pristine graphene, (b) MnO_2 (001), and (c) PDA surfaces. Distribution of the current density vector between anode and cathode with (d) G@PP, (e) MG@PP, and (f) PG@PP. Simulated dendrite growth morphology on (g) G@PP, (h) MG@PP, and (i) PG@PP. (j–l) Insets) Optical and (j–o) SEM images of the graphene-coated layer disassembled from Li–Cu cells after Li deposition with each separator at 0.5 mA cm^{-2} and 1.5 mAh cm^{-2} for three Li deposition/dissolution steps.

inactive sites on the surface compared to a high wettability surface. The distribution of the current density vector (Fig. 5d–f) shows that different wettability levels change the Li-ion flux between the two electrodes. Specifically, the low wettability separator causes the current density to be localized near the inert regions of the separator surface, leading to inhomogeneous Li-ion flux. In contrast, high wettability facilitates the homogeneous transportation of Li-ions toward the anode by resolving the localized current density. Furthermore, the uniform Li-flux resulting from enhanced wettability can also suppress the growth of Li dendrites (Fig. 5g–i). The morphology of Li dendrites changes from sharp to broader shapes with increasing wettability, and dendrite growth is noticeably decreased. This clearly demonstrates that modifying the separator surface with lithiophilic and hydrophilic materials can enhance uniform Li-ion flux, and effectively inhibit the growth of Li dendrites.

The morphology of Li deposition over each separator was evaluated at a density of 0.5 mA cm^{-2} and an areal capacity of 1.5 mAh cm^{-2} . To observe the Li dendrite morphology, Li deposition was performed after three cycles of the Li deposition/dissolution process. Following Li deposition on the G@PP separator, the graphene layer turned yellow, indicating lithiation (Fig. 5j inset). Smudge-like uneven black spots were observed, indicating inhomogeneous deposition of Li. This is more distinctly observed in the top-view SEM images. In the low-magnification image of G@PP, dendritic Li growth is observed at numerous graphene sites, confirming the uneven deposition of Li (Fig. 5j). At high magnification, dendritic Li growth areas are visible, whereas other areas show the original plate-like graphene structure (Fig. 5m). Conversely, photographic images after Li deposition on MG@PP and PG@PP reveal smooth surfaces without smudge-like areas (Fig. 5k and l insets). When observed in low-magnification SEM images, a uniformly distributed graphene plateaus are observed overall (Fig. 5k and l). Additionally, in high-magnification SEM images, a consistent observation of plate-like graphene structures are noted without the presence of dendritic Li regions (Fig. 5n and o). These results indicate that enhanced electrolyte wettability leads to a homogeneous Li-ion flux, which delays the growth of Li dendrites.

To demonstrate the practicality of the developed separators, the Li–S cells were tested at 0.5 C within a potential range of 1.7 – 2.8 V for over 200 cycles after fabrication. Fig. 6a depicts the cycling test outcomes for each cell, providing evidence that Li–S cells with MG@PP and PG@PP

demonstrate superior overall cycling performance compared with cells with PP and those with G@PP. Fig. 6b illustrates the galvanostatic discharge/charge voltage profiles of the Li–S cells. The lithiation process, corresponding to discharge, demonstrates that the plateau around 2.33 V signifies the conversion of ring-like sulfur (S_8) into soluble polysulfides (Li_2S_x , $4 \leq x \leq 8$). Furthermore, the plateau around 2.18 V signifies the conversion reaction of soluble polysulfides (Li_2S_x , $4 \leq x \leq 8$) into insoluble polysulfides (Li_2S_x , $1 \leq x \leq 2$). In the initial cycle, the specific capacities of Li–S cells with MG@PP and PG@PP (1041 and 1042 mAh g^{-1} , respectively) exceed those of cells with PP and G@PP without additional surface modification (872 and 978 mAh g^{-1} , respectively). The polarization gaps in the voltage profiles are detailed in Fig. 6c. PP displays a polarization gap of 403 mV , whereas G@PP exhibits a reduced polarization gap of 315 mV , which is attributed to the effect of reduced local current density and the mitigation of Li volume changes by graphene. With the additional hydrophilic and lithiophilic properties conferred, the polarization gaps of MG@PP and PG@PP are further diminished to 292 mV and 299 mV , respectively, indicating the most reversible reactions. For these reasons, in the 200th cycle, the specific capacities of the Li–S cells with MG@PP and PG@PP are 736 and 789 mAh g^{-1} , respectively, whereas those of the cells with PP and G@PP are 298 and 481 mAh g^{-1} , respectively (Fig. 6a). MG@PP and PG@PP exhibit cycle retention of 71% and 75% at 200 cycles, respectively, compared to 34% for PP and 49% for G@PP. The obtained results are comparable to those in the previous report [45]. The enhanced capacities and cycle retentions in Li–S batteries with surface-modified separators stem from their inherent hydrophilic surfaces, which promote interactions with polysulfides. Furthermore, metal oxides such as MnO_x exhibit catalytic effects on the conversion reactions of Li–S batteries, further boosting cell capacity and retention [46].

4. Conclusions

This study aimed to verify the effect of two different hydrophilic graphene-modifying layers to study how electrolyte wettability and lithiophilicity influence Li deposition behavior in LMBs. MnO_x and PDA were used as functional materials to enhance wettability and lithiophilicity, thus facilitating increased Li-ion pathways and enabling a homogeneous Li-ion flux. In the Li–Cu half cell, after modification, cycle retention showed significant improvement, with 97.7% and 98.9% of

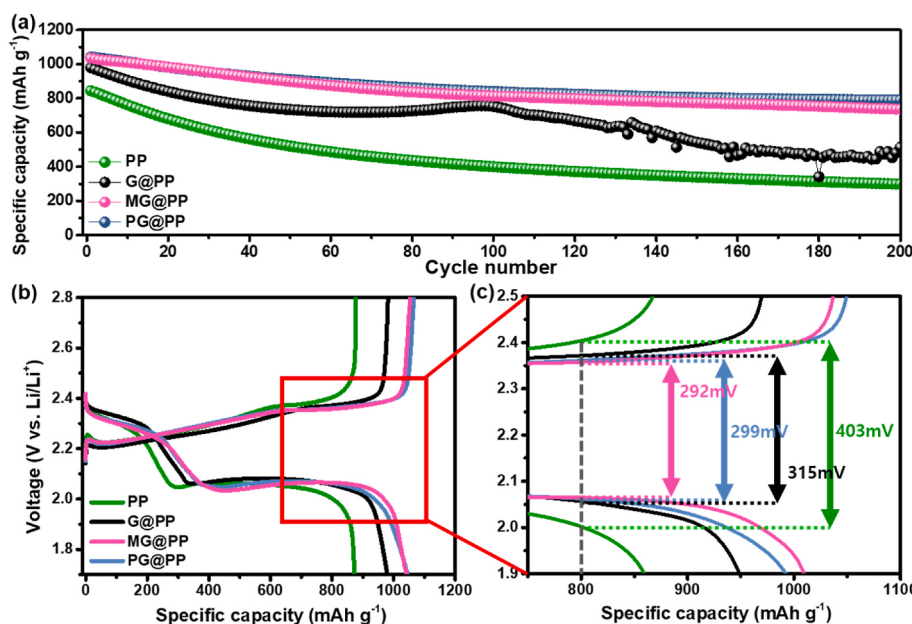


Fig. 6. Evaluation of Li–S full cells. (a) Cycle retention after more than 200 cycles. (b) Voltage profiles of Li–S cells and (c) comparison of polarization gaps of the first cycle.

the initial capacity retained after over 100 cycles for MG@PP and PG@PP, respectively. Electrochemical stability tests under extreme conditions further underscored the strong potential of the modified separators for practical high-loading and high-current LMBs. Inhibited growth of dendritic Li was observed in the top-view SEM image, confirming that the graphene-modified separator with enhanced wettability, immersed with hydrophilic properties influences Li deposition behavior. Furthermore, using DFT and COMSOL analyses, we determined the enhanced lithiophilic properties of each modified material separator. This enhancement, coupled with the hydrophilic characteristics of the material, synergistically promoted a uniform Li-ion flux. Moreover, they exhibited outstanding specific capacities when applied to a Li-S full cell. In comparison to the previous strategy, the coating method simplifies the modification of graphene-coated PP separator surfaces through a few simple steps, leading to enhanced wettability and electrochemical characteristics of LMBs. This study will foster innovative approaches to tackle systemic and practical challenges associated with the use of Li-metal anodes and can be expanded to incorporate other organic/inorganic hydrophilic and lithiophilic materials.

CRediT authorship contribution statement

Wootaeck Choi: Writing – original draft, Visualization, Methodology, Investigation, Formal analysis, Data curation, Conceptualization. **Minsu Park:** Investigation, Formal analysis. **Sujeong Woo:** Investigation, Formal analysis. **Hyunwoo Kim:** Investigation, Data curation. **Min Sung Kang:** Investigation, Formal analysis, Data curation. **Junghyun Choi:** Validation, Resources, Investigation, Data curation. **Sung Beom Cho:** Visualization, Investigation, Data curation. **Taehoon Kim:** Validation, Investigation, Data curation. **Patrick Joohyun Kim:** Writing – review & editing, Validation, Supervision, Resources, Conceptualization.

Declaration of competing interest

The authors declare that they have no known competing financial interests or personal relationships that could have appeared to influence the work reported in this paper.

Acknowledgement

This research was supported by Basic Science Research Program through the National Research Foundation of Korea (NRF) funded by the Ministry of Education (RS-2024-00428511). This research was supported by the National Research Council of Science & Technology (NST) grant by the Korea government (MSIT) (No. GTL24011-000).

Appendix A. Supplementary data

Supplementary data to this article can be found online at <https://doi.org/10.1016/j.carbon.2024.119576>.

References

- [1] M.Z. Jacobson, Review of solutions to global warming, air pollution, and energy security, *Energy Environ. Sci.* 2 (2) (2009) 148–173.
- [2] T.R. Hawkins, O.M. Gausen, A.H. Strømman, Environmental impacts of hybrid and electric vehicles—a review, *Int. J. Life Cycle Assess.* 17 (2012) 997–1014.
- [3] J.B. Goodenough, Y. Kim, Challenges for rechargeable Li batteries, *Chem. Mater.* 22 (3) (2010) 587–603.
- [4] A. Manthiram, Y. Fu, Y.-S. Su, Challenges and prospects of lithium–sulfur batteries, *Accounts of chemical research* 46 (5) (2013) 1125–1134.
- [5] W. Liu, S.W. Lee, D. Lin, F. Shi, S. Wang, A.D. Sendek, Y. Cui, Enhancing ionic conductivity in composite polymer electrolytes with well-aligned ceramic nanowires, *Nat. Energy* 2 (5) (2017) 1–7.
- [6] H. Chen, A. Pei, D. Lin, J. Xie, A. Yang, J. Xu, K. Lin, J. Wang, H. Wang, F. Shi, Uniform high ionic conducting lithium sulfide protection layer for stable lithium metal anode, *Adv. Energy Mater.* 9 (22) (2019) 1900858.
- [7] H. Chen, Y. Yang, D.T. Boyle, Y.K. Jeong, R. Xu, L.S. de Vasconcelos, Z. Huang, H. Wang, H. Wang, W. Huang, Free-standing ultrathin lithium metal-graphene oxide host foils with controllable thickness for lithium batteries, *Nat. Energy* 6 (8) (2021) 790–798.
- [8] L. Chen, X. Fan, X. Ji, J. Chen, S. Hou, C. Wang, High-energy Li metal battery with lithiated host, *Joule* 3 (3) (2019) 732–744.
- [9] M.D. Tikekar, S. Choudhury, Z. Tu, L.A. Archer, Design principles for electrolytes and interfaces for stable lithium–metal batteries, *Nat. Energy* 1 (9) (2016) 1–7.
- [10] P.J. Kim, K. Kim, V.G. Pol, Uniform metal-ion flux through interface-modified membrane for highly stable metal batteries, *Electrochim. Acta* 283 (2018) 517–527.
- [11] L. Fan, H.L. Zhuang, W. Zhang, Y. Fu, Z. Liao, Y. Lu, Stable lithium electrodeposition at ultra-high current densities enabled by 3D PMF/Li composite anode, *Adv. Energy Mater.* 8 (15) (2018) 1703360.
- [12] J. Choi, P.J. Kim, A roadmap of battery separator development: past and future, *Curr. Opin. Electrochem.* 31 (2022) 100858.
- [13] T.W. Zhang, J.L. Chen, T. Tian, B. Shen, Y.D. Peng, Y.H. Song, B. Jiang, L.L. Lu, H. B. Yao, S.H. Yu, Sustainable separators for high-performance lithium ion batteries enabled by chemical modifications, *Adv. Funct. Mater.* 29 (28) (2019) 1902023.
- [14] C. Xue, D. Jin, H. Nan, H. Wei, H. Chen, S. Xu, A novel polymer-modified separator for high-performance lithium-ion batteries, *J. Power Sources* 449 (2020) 227548.
- [15] C. Yang, H. Tong, C. Luo, S. Yuan, G. Chen, Y. Yang, Boehmite particle coating modified microporous polyethylene membrane: a promising separator for lithium ion batteries, *J. Power Sources* 348 (2017) 80–86.
- [16] T. Lei, W. Chen, W. Lv, J. Huang, J. Zhu, J. Chu, C. Yan, C. Wu, Y. Yan, W. He, Inhibiting polysulfide shuttling with a graphene composite separator for highly robust lithium-sulfur batteries, *Joule* 2 (10) (2018) 2091–2104.
- [17] E.C. Cengiz, O. Salihoglu, O. Ozturk, C. Kocabas, R. Demir-Cakan, Ultra-lightweight chemical vapor deposition grown multilayered graphene coatings on paper separator as interlayer in lithium-sulfur batteries, *J. Alloys Compd.* 777 (2019) 1017–1024.
- [18] P.J. Kim, V.G. Pol, High performance lithium metal batteries enabled by surface tailoring of polypropylene separator with a polydopamine/graphene layer, *Adv. Energy Mater.* 8 (36) (2018) 1802665.
- [19] M.F. El-Kady, Y. Shao, R.B. Kaner, Graphene for batteries, supercapacitors and beyond, *Nat. Rev. Mater.* 1 (7) (2016) 1–14.
- [20] K. Kwon, J. Kim, K. Roh, P.J. Kim, J. Choi, Towards high performance Li metal batteries: surface functionalized graphene separator with improved electrochemical kinetics and stability, *Electrochim. Commun.* 157 (2023) 107598.
- [21] R. Fang, K. Chen, L. Yin, Z. Sun, F. Li, H.M. Cheng, The regulating role of carbon nanotubes and graphene in lithium-ion and lithium–sulfur batteries, *Adv. Mater.* 31 (9) (2019) 1800863.
- [22] M. Park, S. Woo, J. Seo, J. Choi, E. Jeong, P.J. Kim, Directing the uniform and dense Li deposition via graphene-enhanced separators for high-stability Li metal batteries, *Electrochim. Acta* (2024) 144426.
- [23] K. Dujeacic-Stephane, M. Gupta, A. Kumar, V. Sharma, S. Pandit, P. Bocchetta, Y. Kumar, The effect of modifications of activated carbon materials on the capacitive performance: surface, microstructure, and wettability, *Journal of Composites Science* 5 (3) (2021) 66.
- [24] J. Feng, Z. Guo, Wettability of graphene: from influencing factors and reversible conversions to potential applications, *Nanoscale Horizons* 4 (2) (2019) 339–364.
- [25] S. Wang, Y. Zhang, N. Abidi, L. Cabrales, Wettability and surface free energy of graphene films, *Langmuir* 25 (18) (2009) 11078–11081.
- [26] W. Zhang, Z. Tu, J. Qian, S. Choudhury, L.A. Archer, Y. Lu, Design principles of functional polymer separators for high-energy, metal-based batteries, *Small* 14 (11) (2018) 1703001.
- [27] D.H. Jeon, Enhancing electrode wettability in lithium-ion battery via particle-size ratio control, *Appl. Mater. Today* 22 (2021) 100976.
- [28] H. Huo, X. Li, Y. Chen, J. Liang, S. Deng, X. Gao, K. Doyle-Davis, R. Li, X. Guo, Y. Shen, Bifunctional composite separator with a solid-state-battery strategy for dendrite-free lithium metal batteries, *Energy Storage Mater.* 29 (2020) 361–366.
- [29] J. Yu, Y. He, S. Zou, B. Na, H. Liu, J. Liu, H. Li, Redox-active manganese dioxide@polypropylene hybrid separators for advanced lithium ion batteries, *Appl. Surf. Sci.* 508 (2020) 144757.
- [30] V.C. Ho, B.T.D. Nguyen, H.Y.N. Thi, J.F. Kim, J. Mun, Poly (dopamine) surface-modified polyethylene separator with electrolyte-philic characteristics for enhancing the performance of sodium-ion batteries, *Int. J. Energy Res.* 46 (4) (2022) 5177–5188.
- [31] Y. Liu, K. Ai, L. Lu, Polydopamine and its derivative materials: synthesis and promising applications in energy, environmental, and biomedical fields, *Chemical reviews* 114 (9) (2014) 5057–5115.
- [32] G. Yu, Q. Zhao, W. Wu, X. Wei, Q. Lu, A facile and practical biosensor for choline based on manganese dioxide nanoparticles synthesized in-situ at the surface of electrode by one-step electrodeposition, *Talanta* 146 (2016) 707–713.
- [33] Y. Suharto, Y. Lee, J.-S. Yu, W. Choi, K.J. Kim, Microporous ceramic coated separators with superior wettability for enhancing the electrochemical performance of sodium-ion batteries, *J. Power Sources* 376 (2018) 184–190.
- [34] Y. Xie, H. Xiang, P. Shi, J. Guo, H. Wang, Enhanced separator wettability by LiTFSI and its application for lithium metal batteries, *J. Membr. Sci.* 524 (2017) 315–320.
- [35] H. Park, D.H. Yeom, J. Kim, J.K. Lee, MnO/C nanocomposite prepared by one-pot hydrothermal reaction for high performance lithium-ion battery anodes, *Kor. J. Chem. Eng.* 32 (2015) 178–183.
- [36] Z. Gong, C. Lian, P. Wang, K. Huang, K. Zhu, K. Ye, J. Yan, G. Wang, D. Cao, Lithiophilic Cu-Li₂O matrix on a Cu collector to stabilize lithium deposition for lithium metal batteries, *Energy & Environmental Materials* 5 (4) (2022) 1270–1277.

- [37] M.-L. Zhou, Z. Zhang, J. Xu, J. Wei, J. Yu, Z.-Y. Yang, PDA modified commercial paper separator engineering with excellent lithiophilicity and mechanical strength for lithium metal batteries, *J. Electroanal. Chem.* 868 (2020) 114195.
- [38] G. Kresse, J. Furthmüller, Efficient iterative schemes for ab initio total-energy calculations using a plane-wave basis set, *Physical review B* 54 (16) (1996) 11169.
- [39] P.E. Blöchl, Projector augmented-wave method, *Physical review B* 50 (24) (1994) 17953.
- [40] J.P. Perdew, K. Burke, M. Ernzerhof, Generalized gradient approximation made simple, *Phys. Rev. Lett.* 77 (18) (1996) 3865.
- [41] D. Guo, Z. Hu, Q. Li, L. Bian, Y. Song, X. Liu, Mixed-valence manganese oxide/reduced graphene oxide composites with enhanced pseudocapacitive performance, *J. Mater. Sci.* (2022) 1–13.
- [42] H. Hemmatpour, O. De Luca, D. Crestani, M.C. Stuart, A. Lasorsa, P.C. van der Wel, K. Loos, T. Giousis, V. Haddadi-Asl, P. Rudolf, New insights in polydopamine formation via surface adsorption, *Nat. Commun.* 14 (1) (2023) 664.
- [43] J. Zhong, F. Yi, A. Gao, D. Shu, Y. Huang, Z. Li, W. Zhu, C. He, T. Meng, S. Zhao, Preparation of 3D reduced graphene oxide/MnO₂ nanocomposites through a vacuum-impregnation method and their electrochemical capacitive behavior, *Chemelectrochem* 4 (5) (2017) 1088–1094.
- [44] W. Cai, C. Yan, Y.X. Yao, L. Xu, X.R. Chen, J.Q. Huang, Q. Zhang, The boundary of lithium plating in graphite electrode for safe lithium-ion batteries, *Angew. Chem. Int. Ed.* 60 (23) (2021) 13007–13012.
- [45] K. Kim, P.J. Kim, J.P. Youngblood, V.G. Pol, Surface functionalization of carbon architecture with nano-MnO₂ for effective polysulfide confinement in lithium–sulfur batteries, *ChemSusChem* 11 (14) (2018) 2375–2381.
- [46] W.G. Lim, S. Kim, C. Jo, J. Lee, A comprehensive review of materials with catalytic effects in Li–S batteries: enhanced redox kinetics, *Angew. Chem. Int. Ed.* 58 (52) (2019) 18746–18757.